

Article

Transport of Oxygen-Doped Graphitic Carbon Nitride in Saturated Sand: Effects of Concentration, Grain Size, and Ionic Strength

Thanh-Tuan Nguyen ¹ , Do-Gun Kim ^{2,*}  and Seok-Oh Ko ^{1,*} 

¹ Department of Civil Engineering, Kyung Hee University, 1732, Deakyeongdaero, Yongin 17104, Gyeonggi-do, Republic of Korea; nguyentuan@khu.ac.kr

² Department of Environmental Engineering, Suncheon National University, 255 Jungang-ro, Suncheon 57922, Jeollanam-do, Republic of Korea

* Correspondence: dgkim@scnu.ac.kr (D.-G.K.); soko@khu.ac.kr (S.-O.K.); Tel.: +82-61-750-3817 (D.-G.K.); +82-31-201-2999 (S.-O.K.); Fax: +82-61-750-3810 (D.-G.K.); +82-31-202-8854 (S.-O.K.)

Abstract: In this study, the characteristics and transport of oxygen-doped graphitic carbon nitride (OgCN) were investigated in comparison with multi-walled carbon nanotube (MWCNT), and the transport of OgCN was evaluated under various conditions. OgCN was superior to MWCNT in transport within a quartz sand layer with less attachment and more detachment than MWCNT, which is attributable to more diverse and abundant functional groups, charges, defects, and amorphous graphitic structures. OgCN transport was well described by a one-dimensional advection–dispersion–retention model. The coefficients of retention (S_{max}), attachment (k_a), and detachment (k_d) calculated by the model were not always well-correlated with OgCN concentration and the grain size of the medium, suggesting that the OgCN transport was affected by various factors such as attachment, detachment, and pore size. However, it was clearly and significantly inhibited by ionic strength, via improved aggregation of OgCN. It is believed that the results of this study contribute to establish proper sub-surface injection strategies of carbonaceous materials for in situ chemical oxidation.

Keywords: oxygen-doped graphitic carbon nitride; column experiment; breakthrough curves; transport modeling



Citation: Nguyen, T.-T.; Kim, D.-G.; Ko, S.-O. Transport of Oxygen-Doped Graphitic Carbon Nitride in Saturated Sand: Effects of Concentration, Grain Size, and Ionic Strength. *Water* **2024**, *16*, 6. <https://doi.org/10.3390/w16010006>

Academic Editors: Yunhui Zhang, Qili Hu and Liting Hao

Received: 29 November 2023

Revised: 14 December 2023

Accepted: 16 December 2023

Published: 19 December 2023



Copyright: © 2023 by the authors. Licensee MDPI, Basel, Switzerland. This article is an open access article distributed under the terms and conditions of the Creative Commons Attribution (CC BY) license (<https://creativecommons.org/licenses/by/4.0/>).

1. Introduction

In situ chemical oxidation (ISCO), which uses various oxidants, including hydrogen peroxide (H_2O_2), peroxydisulfate ($S_2O_8^{2-}$, PDS), peroxymonosulfate (HSO_5^- , PMS), and permanganate (MnO_4^- , PM), is an efficient and economical option for the removal of organic pollutants from soil and groundwater via oxidative degradation, limiting the spread of pollutants and their associated risks [1–3]. The ISCO is based on the oxidative degradation of organic pollutants by the attack of radical and/or non-radical reactive species, such as $\bullet OH$, $SO_2\bullet^-$, and 1O_2 , via the activation of the oxidants [4,5]. The activation is carried out using various homogeneous and heterogeneous catalysts and activators.

Homogeneous activators and/or catalysts include transition metal ions, most frequently Fe^{2+} , heat, UV, and ultrasound [6–8]. However, those homogeneous processes have critical drawbacks in subsurface applications, such as high cost, limited large-scale applications, blockage of pores in aquifers via the formation of metal precipitates, and secondary pollution by the migration of metals to clean zones [9,10].

Therefore, the use of heterogeneous catalysts such as solid-phase zero-valence metals, metal (hydr)oxides, metal-free carbonaceous materials, and composites can be beneficial in ISCO. These heterogeneous catalysts and/or activators have a broader range of working pH, are easily recovered, can be regenerated, and have a wider application via modification of the reactive sites on them [11,12]. Among the heterogeneous catalysts, metal-containing

materials have the inherent disadvantage of metal leaching, which causes secondary pollution, pore blocking, and the deactivation of the catalysts via migration, as well as the formation and accumulation of less reactive metal species [13–17]. On the other hand, the risks of metal-containing materials are avoided by using metal-free carbonaceous materials, such as graphene oxide (GO), cubic mesoporous carbon, carbon nanotubes (CNTs), nanodiamonds, graphitic carbon nitride (gCN), and activated carbon (AC). They have excellent thermal and chemical stability, availability, and well-developed meso- and micro-pores, which can provide more surface-reactive sites [13]. Therefore, carbonaceous materials can be good options for use as catalysts in ISCO and have been the focus of recent research [14].

Other than the high potential of the carbonaceous materials as catalysts in ISCO, it must be noted that the transport of the materials in the subsurface environment is critical for their successful application in ISCO [2,11]. A catalyst and/or activator must be transported through the pores of soil layers and spread readily throughout the contaminated zone [2,11,17]. The transport is more difficult for solid materials than dissolved ions, such as Fe^{2+} [2,11]. However, limited numbers of publications have investigated the transport of heterogeneous catalytic materials through porous media, such as aquifers.

In this regard, the transport of a metal-free carbonaceous material, which is one of the good candidates for catalysts for ISCO, was investigated in this study to establish a proper strategy for its injection into subsurface-contaminated zones. Oxygen-doped gCN (OgCN) was selected as the catalyst. OgCN has a graphene-like layered structure and is prepared using cheap materials, such as urea and oxalic acid, via replacing N atoms in the amino groups in the heptazine units of gCN [18]. The high potential of the OgCN in ISCO can be justified by the remediation efficiency and safety.

Both gCN and OgCN are good photocatalysts [18–21]. However, OgCN demonstrates effective PMS activation, an effect that is negligible in gCN [18,19]. It was suggested that the electron-rich O and the electron-poor C atoms near the O accelerated the electron transfer from organic pollutants (electron donor) to PMS (electron acceptor), and the generation of reactive species, such as $\text{SO}_2^{\bullet-}$ and $^1\text{O}_2$, eventually enhanced the oxidative degradation of the organic pollutants [14,18,19]. For example, OgCN was excellent in the degradation of bisphenol-A (BPA) and oxytetracycline via PMS activation to generate $\bullet\text{OH}$, $\text{SO}_2^{\bullet-}$, and $^1\text{O}_2$ [18,19]. Moreover, OgCN is also an efficient photocatalyst for BPA degradation via improved charge-carriers separation and changing the positions of valance and conduction bands [20,21]. In addition, gCNs are non-toxic [18], so the residual OgCN after the operation of ISCO does not cause a risk in the underground environment. First, the properties and transport of OgCN in a porous medium were compared with those of multi-walled carbon nanotubes (MWCNT), to identify the effects of the material characteristics on transport. Then, the transport of OgCN was evaluated under various OgCN concentrations, grain sizes of the medium, and ionic strength (IS).

2. Materials and Methods

2.1. Materials

The OgCN was synthesized from a mixture of urea and oxalic acid via one-step thermal treatment [21]. In detail, 20 g of urea and 8 g of oxalic acid were mixed and ground for 30 min. Then, the mixture was heated in a box furnace at 550 °C for 4 h at a ramp rate of 3 °C/min. It was shown that the doped O substitutes the graphitic- and pyridinic-N to increase the electron-rich O atoms and the electron-poor C atoms near the O, in OgCN [18,21]. The obtained brown powders were cooled to room temperature, ground, and stored until use. MWCNTs and graphite flakes were purchased from Carbon Nano-material Technology Co., Ltd. (Pohang, Republic of Korea) and Alfa Aesar (Ward Hill, MA, USA), respectively. They were rinsed with de-ionized (DI) water 10 times before drying at 105 °C for 24 h.

Standard sand (ISO 679, SNL Corp., Leucate, France) was used as the porous media. It was separated into two size ranges, 0.25–0.6 mm and 0.6–1.0 mm, by sieving. They were treated sequentially with 0.1 M of H_2SO_4 to remove metal oxides, and then 5% of H_2O_2 to

remove organic materials on the surfaces [22]. They were then rinsed with DI water until the pH was 7.0 ± 0.2 and dried in an oven at 105°C for 24 h.

2.2. Characterization

The crystal structure of the materials was analyzed via X-ray diffraction (XRD) using an X-ray Diffractometer (D8 Advance, Bruker, Germany) at a 2θ range of 3° to 89.14° and scanning speed of $0.2^\circ/\text{min}$, using Cu $K\alpha$ radiation. The Raman spectra were recorded with an inVia Raman microscope (Renishaw, UK). The excitation wavelength was 514 nm, the spectral resolution was 4 cm^{-1} , the exposure time was 10 s, and the total acquisitions was 20. Fourier-transform infrared spectroscopy (FTIR) spectra were obtained using the Spectrum One system (Perkin-Elmer, Shelton, CT, USA) to determine the surface functional groups. The pellet was prepared using the ground mixtures of 200 mg of KBr with 0.2 g of OgCN or MWCNT. The spectra were recorded for 8 successive scans at the wavelengths of $4000\text{--}400\text{ cm}^{-1}$, with a resolution of 4 cm^{-1} . The element chemical states on the surfaces of the catalysts were obtained via X-ray photoelectron spectroscopy (XPS) with K-Alpha (Thermo Electron, Waltham, MA, USA). A monochromatic Al α -Alpha radiation source was used and the spot diameter was $400\text{ }\mu\text{m}$. The high-resolution XPS spectra were recorded for C1s, N1s, and O1s for 10 scans (0.1 eV steps) and with 30 eV of pass energy. The particle size distribution (PSD) was determined via dynamic light scattering (DLS) using a Zetasizer nanoseries (Zen 3600 Zetasizer Nano ZS, Particle Size Analyzer, Malvern Instruments, Malvern, UK) and the zeta potential of OgCN at different ionic strength (IS) concentrations (0, 2, 5, and 10 mM, pH 7) was determined using a Zeta Potential Analyzer (Brookhaven Instruments Corporation, Holtsville, NY, USA). The 5 g/L suspensions of OgCN or MWCNT were prepared in 0.01 M KCl aqueous solution and the pH was in a range from 2 to 10.

2.3. Column Experiments

The aqueous suspension of OgCN, MWCNT, or graphite was prepared by mixing 500 mg of OgCN in 1 L of DI water (Aquapuri 5-Super Water Purification System, Youngin Chromass, Anyang, Republic of Korea), and sonicated for 60 min to avoid aggregation. The pH of the suspension was adjusted to 7.0 ± 0.2 with 0.1 M HCl and 0.1 M NaOH.

A glass column of 25 mm inner diameter and 145 mm length, equipped with two end plates with stainless steel screens, was filled with the ISO sands. The packing densities were 1.43 and 1.5 g/cm^2 , the pore volumes were 23 and 24 mL, and the porosities were 0.38 and 0.44 when the column was filled with sands of $0.25\text{--}0.6\text{ mm}$ and $0.6\text{--}1.0\text{ mm}$, respectively. The tracer breakthrough test was carried out using 1 M of KCl (Daejung Chemicals, Siheung, Republic of Korea) solution at a flow rate of 5 mL/min to estimate the longitudinal dispersity [22]. The concentration of KCl was determined with a conductivity meter (LabQuest 2, Vernier Software & Technology LLC, Beaverton, OR, USA).

The transport of OgCN was investigated via the pulse injection method. The sand-filled column was flushed with 40 pore volumes (PVs) of the DI water. Then, 4 PVs of the OgCN suspension were injected into the saturated column for 22 min. It was quickly switched into DI water, and the flow was maintained until no OgCN was detected. The suspension and the DI water were injected using a peristaltic pump (LeadFluid-BT301L, Baoding Lead Fluid Technology Co., Ltd., Baoding, China), at a constant flow rate of 5 mL/min .

The effluent from the column was collected at predetermined intervals. The concentration of the OgCN and graphite of the samples was measured using a UV-Vis spectrophotometer (UVmini-1240, Shimadzu Corporation, Kyoto, Japan) at a wavelength of 500 nm [23], while that of MWCNT was determined at 400 nm [22].

2.4. Modeling

The results of transport experiments, i.e., the concentration of OgCN or MWCNT in the effluents of the columns at a predetermined time, were analyzed using the HYDRUS

1D software package. HYDRUS 1D is based on the advection–dispersion equation (ADE) via breakthrough curves (BTCs) of OgCN or MWCNT at different conditions to model transport and retention in the column [24]. The governing equations in this simulation are provided in Equations (1)–(3) [25]:

$$\theta \frac{\partial C}{\partial t} = \theta D \frac{\partial^2 C}{\partial x^2} - q \frac{\partial C}{\partial x} - \rho \frac{\partial S}{\partial t} \quad (1)$$

$$\rho \frac{\partial S}{\partial t} = \theta k_a \Psi C - k_d \rho S \quad (2)$$

$$\Psi = \left(1 - \frac{S}{S_{max}}\right) \left(\frac{d_c + x}{d_c}\right)^{-\beta} \quad (3)$$

where C is the OgCN concentration in the influent (mg L^{-1}); S is the solid phase OgCN concentration trapped in the media (mg g^{-1}); t is the time passed (min); D is the dispersion coefficient (cm min^{-1}); x is the travel distance (cm); θ is the porosity; ρ is the bulk density of sand (g cm^{-3}); q is the Darcy velocity (cm min^{-1}); S_{max} is the maximum retention of OgCN concentration on sand (mg g^{-1}); k_a is the first-order attachment coefficient (min^{-1}); k_d is the first-order detachment coefficient (min^{-1}); d_c is the medium grain size (cm); Ψ is the dimensionless function; and β is an empirical factor (with 0.43 as an ideal value) [24].

3. Results and Discussion

3.1. Comparisons of OgCN and MWCNT

3.1.1. Transport

The transports of OgCN and MWCNT were compared first, to investigate the differences between OgCN and MWCNT in relation to their properties. Figure 1 shows that the transport of OgCN was much better than that of MWCNT. Their transport recovery percentages were 76% and 18%, respectively. The maximum retention (S_{max}) of OgCN was higher (3.3527 mg g^{-1}) than that of MWCNT (2.6913 mg g^{-1}), and the k_a of OgCN (0.1514 min^{-1}) was around 31% of that of MWCNT (0.4886 min^{-1}). However, the k_d of OgCN (0.0052 min^{-1}) was 4.7 times higher than that of MWCNT (0.0011 min^{-1}), suggesting that the better transport of OgCN, compared with MWCNT, was more attributable to its superior detachment rather than a decreased attachment. In addition, it was found in the experiments that MWCNT was readily aggregated into larger particles when it was pumped out from the tank of the suspension, which was mixed for the whole of the period of experiments; in other words, when the mixing was stopped. This result is probably because of the intrinsically high hydrophobicity, which caused the MWCNT to mostly accumulate near the inlet of the column.

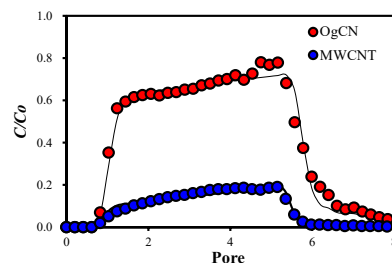


Figure 1. Experimental and modeling breakthrough curves of OgCN and MWCNT. [OgCN] = [MWCNT] = 50 mg L^{-1} , flow rate = 5 mL min^{-1} , pH = 7 ± 0.2 , grain size = $0.6\text{--}1.0 \text{ mm}$.

3.1.2. Characteristics

The superior transport of OgCN relative to MWCNT was investigated further with respect to their properties. The FTIR spectra of OgCN and MWCNT showed common bands at ~ 3430 , $\sim 2917/2849$, and $\sim 1623 \text{ cm}^{-1}$, which can be assigned to the stretching vibrations of N–H/O–H, C–H, and aromatic C=C bonds, respectively. However, more

bands were found for OgCN at 1418, 1318, and 1255 cm^{-1} representing C=O, C–N, and C–O in CN heterocycles, respectively [21,26]. In addition, a clear band was found at 810 cm^{-1} , which corresponds to the triazine units of gCNs [21] (Figure 2A).

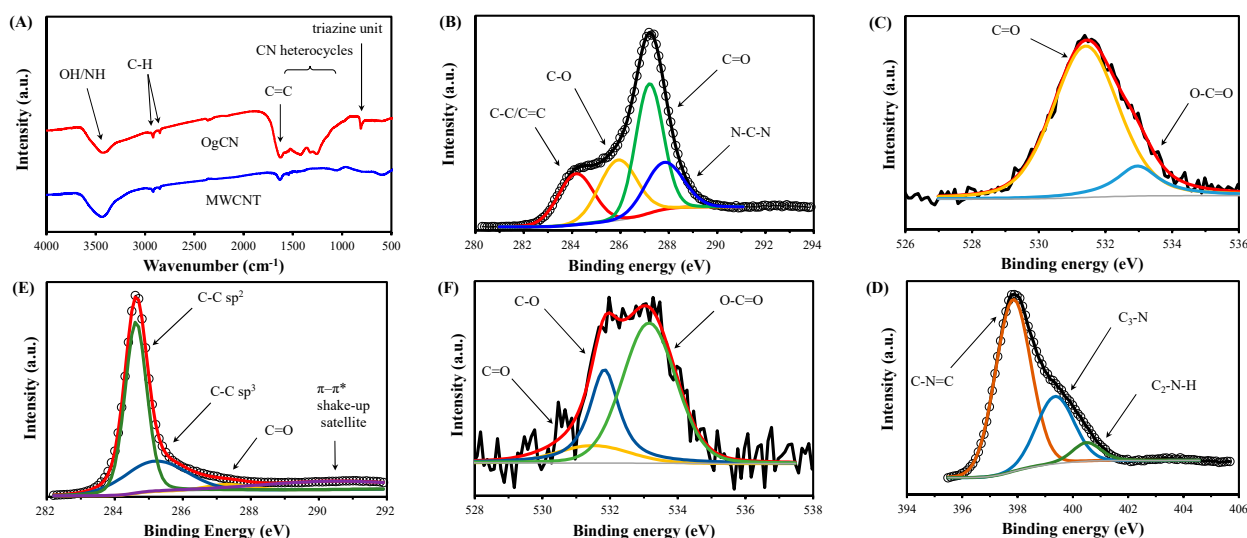


Figure 2. Results of (A) FTIR spectroscopy of OgCN and MWCNT; (B) C1s, (C) O1s, and (D) N1s XPS of OgCN; and (E) C1s and (F) O1s XPS of MWCNT.

The atomic fractions of C, N, and O were 47.2%, 49.06%, and 3.74%, respectively, for OgCN, while they were 98.89%, 0.26%, and 0.85%, respectively for MWCNT, demonstrating a CN structure and the successful doping of O in OgCN and the high purity of MWCNT, respectively. The (O + N)/C of OgCN (1.12) was much higher than that of MWCNT (0.01), indicating a greater hydrophilicity of OgCN than MWCNT. The high-resolution XPS spectra are presented in Figure 2B–F. The C1s, O1s, and N1s spectra were deconvoluted into characteristic peaks using XPS peak 4.1 software (Table 1) [27]. The C1s XPS spectrum of OgCN showed the peaks of graphitic C–C/C=C, C–O, C=O, and N–C–N at 284.2, 285.9, 287.2, and 287.8 eV, respectively, as assigned in previous works related to gCNs [28,29]. On the other hand, in the C1s XPS spectrum of MWCNT, the peaks of sp^2 -C and sp^3 -C, at 284.6 and 285.2 eV, respectively [28,29], were clearly separated, and the peaks of C–O and N–C–N were absent. The C=O peak was dominant in the O1s XPS spectrum of OgCN, while MWCNT’s O1s XPS spectrum showed low-intensity peaks of C=O, C–O, and O–C=O [28]. The N1s spectrum of OgCN consisted of peaks corresponding to C–N=C, C_3 -N, and C_2 -N–H, at 397.8, 399.4, and 400.5 eV, respectively, as also reported in previous works about CNs [28,29].

Table 1. XPS results of OgCN and MWCNT.

		C1s				O1s				N1s				
		C–C/ C=C	C–C, sp^2	C–C sp^3	C–O	C=O	N–C–N	Π - Π^* Shake-up Satellite	C=O	C–O	O–C=O	C–N=C	C_3 -N	C_2 -N–H
OgCN	Position (eV)	284.2			285.9	287.2	287.8		531.4		533.0	397.8	399.4	400.5
	Fraction (%)	9.2			11.2	17.9	8.8		3.2		0.6	32.7	13.3	3.1
	FWHM (eV)	1.7			1.9	1.3	1.9		2.3		1.5	1.5	1.6	1.2
MWCNT	Position (eV)		284.6	285.2		287.3		290.5	531.5	531.8	533.2			
	Fraction (%)		53.3	25.3		3.3		17.0	0.1	0.3	0.5			
	FWHM (eV)		0.8	2.2		1.5		5.1	2.5	1.0	1.9			

The XRD patterns of OgCN and MWCNT showed common peaks in the (100) plane for in-plane graphitic structures (13.4°) and in the (002) plane for inter-layer stacking [21] (Figure 3A). However, the diffraction angle of OgCN (27.6°) was higher than that of MWCNT (26.5°), indicating that the interlayer stacking was more severe in OgCN than in MWCNT [30]. This suggests that OgCN has a better tribological property, i.e., higher

wear resistance and lower friction, than MWCNT, which would facilitate easier transport through the pores of a medium with less resistance [31].

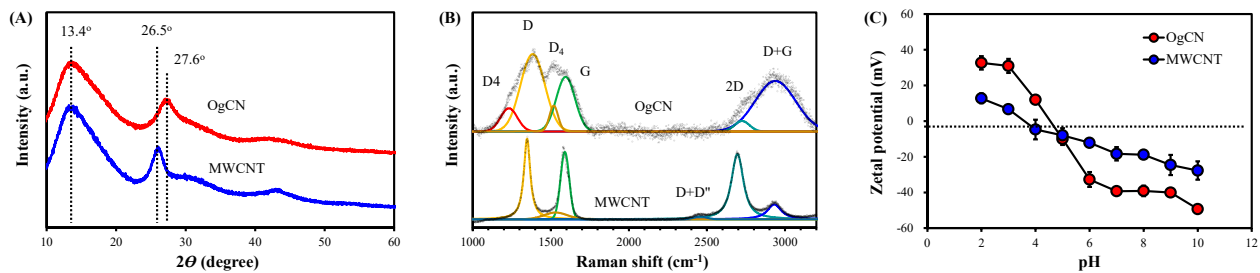


Figure 3. The (A) XRD patterns, (B) Raman spectra, and (C) zeta potential of OgCN and MWCNT.

The D4-, D-, D₄-, G-, 2D-, and D + G bands were found in the Raman spectrum of OgCN at 1232, 1384, 1519, 1595, 2724, and 2938 cm⁻¹, respectively (Figure 3B) (Table 2). The D4-band represents the disordered graphitic lattice, ionic impurities, and polyenes, while D-, D₄-, G-, 2D-, and D + G bands are associated with disordered structures such as defects and edges, amorphous carbon, ideal lattice of graphitic structures, single graphene-like layers, and a combination of the D and G bands, respectively [32,33]. The D4-band was not found, while a small D + D''-band was found at 2458 cm⁻¹ in the Raman spectrum of MWCNT, which is assigned to the combination of the D-band and the D''-band representing amorphous carbon. On the other hand, the ratio of the intensity of the D-band to the G-band (I_D/I_G) represents the relative abundance of defects in graphitic structures, while the ratio of the intensity of the 2D-band to the G-band (I_{2D}/I_G) is indicative of the relative abundance of single-layer graphene and is inversely proportional to the degree of stacking of graphitic layers [32]. It was shown that I_D/I_G was higher for OgCN (1.83) than for MWCNT (1.81), while the I_{2D}/I_G was greatly larger for MWCNT than for OgCN. The results show that, compared with that in MWCNT, the graphitic structure in OgCN is characterized by more defects, either structural or by impurity, more amorphous structures, less ideal graphitic planes, less single-layer graphene-like structures, and a much greater degree of stacking, which is also suggested in XRD patterns (Figure 3A).

Table 2. Raman spectroscopy results of OgCN and MWCNT.

		D4	D	D ₄	G	D + D''	2D	D + G	I_D/I_G	I_{2D}/I_G
OgCN	Center (cm ⁻¹)	1232	1384	1519	1595		2724	2938	1.83	0.15
	Area (%)	6.8	32.8	4.1	17.9		2.8	35.6		
	FWHM (cm ⁻¹)	127.2	182.9	65.8	141.4		113.1	304.1		
MWCNT	Center (cm ⁻¹)		1348	1531	1590	2458	2695	2932	1.31	1.89
	Area (%)		26.0	5.3	19.8	1.2	37.5	10.2		
	FWHM (cm ⁻¹)		48.9	175.7	64.9	94.4	91.6	106.8		

The zeta potential of OgCN and MWCNT are provided in Figure 3C. The points of zero charge (pH_{pzc}) were around 3.6 and 4.6 for MWCNT and OgCN, respectively. The absolute values of zeta potential were higher for OgCN than for MWCNT, at pHs of 2–4 and >5. This indicates that OgCN contains more acidic and/or basic functional groups than MWCNT [34]. This is also suggested by the FTIR spectra and XPS spectra, which show that OgCN was more abundant in O-, N-, and C-containing groups such as C=O, C–N, and C–O, than MWCNT (Figure 2).

Collectively, OgCN was less crystalline, more stacked, and more negatively charged at the pH of this study (7.0), richer in O- and/or N-containing functional groups, and more abundant in structural defects, than MWCNT. These properties are beneficial for transport in porous media, providing more charges and hydrophilicity. It was reported that a

modified MWCNT, enriched with O-containing functional groups such as carboxylic groups via refluxing with HNO₃, showed enhanced transport relative to pristine MWCNT [35]. The enhanced transport of a material achieved by enriching functional groups was also demonstrated for single-wall CNTs (SWCNTs). The transport in quartz sand columns was better for humic-acid-modified SWCNTs than for oxidized SWCNTs because of more abundant functional groups, which provide more negative charges [36].

3.2. Transport of OgCN under Various Conditions

The transport of OgCN was investigated under varying OgCN concentrations, medium grain sizes, and IS. All results were analyzed using HYDRUS-1D (Equations (1)–(3)), which provided good fits to the experimental results, except for when IS was extremely high (10 mM KCl). The calculated parameters for each condition are presented in Table 3, and the results are discussed separately thereafter.

Table 3. Experimental conditions and parameters of HYDRUS-1D.

	Concentration (mg L ⁻¹)	Grain Size (mm)	IS (mM KCl)	k_a (min ⁻¹)	k_d (min ⁻¹)	S_{max} (mg g ⁻¹)	r^2
OgCN	10	0.25–0.6	0	0.1831	0.0029	2.76	0.950
	50	0.25–0.6	0	0.1920	0.0086	3.73	0.954
	100	0.25–0.6	0	0.3468	0.0033	4.30	0.916
	10	0.6–1.0	0	0.1850	0.0023	2.56	0.948
	50	0.6–1.0	0	0.1514	0.0052	3.35	0.973
	100	0.6–1.0	0	0.0936	0.0115	3.57	0.981
	50	0.6–1.0	2	0.2458	0.0001	3.81	0.933
	50	0.6–1.0	5	0.4160	0.0017	4.56	0.927
	50	0.6–1.0	10	0.6190	0.0005	5.74	0.885
MWCNT	50	0.6–1.0	0	0.4876	0.0023	2.69	0.975
	50	0.6–1.0	10	0.4886	0.0011	3.43	0.963

3.2.1. Effects of OgCN Concentration and the Grain Size of the Medium

Figure 4 shows the breakthrough curves of OgCN with respect to the passed pore volume at different OgCN concentrations and the grain size of the packed quartz sand. The k_a , k_d , and S_{max} are presented with respect to the OgCN concentrations in Figure 5.

The S_{max} increased with increasing OgCN concentration for both 0.25–0.6 and 0.6–1.0 mm sand, indicating that the retention is significantly affected by the influent amount. However, the increase in S_{max} was not as significant as the increase in OgCN concentration. The S_{max} was increased 1.56 (2.76 to 4.30 mg/g) and 1.40 (2.56 to 3.57 mg/g) times for the 0.25–0.6 mm and 0.6–1.0 mm sand columns, respectively, when the OgCN concentration was increased 10 times, i.e., from 10 mg/L to 100 mg/L. This suggests that not only the attachment, but also the detachment played an important role in the transport of OgCN, and that increased injection of OgCN is not necessarily followed by greater retention.

The k_a was decreased from 0.1850 to 0.0936 min⁻¹, while k_d was increased from 0.0023 to 0.0115 min⁻¹, as the OgCN concentration was increased in 0.6–1.0 mm sand, indicating that some of the OgCN retained in the quartz sand was detached. However, it is also shown that k_a and k_d were at their highest when OgCN concentrations were 100 and 50 mg/L, respectively, in 0.25–0.6 mm sand, having a lower porosity (0.38) than 0.6–1.0 mm sand (0.44). The different attachment and detachment values of OgCN indicate that they were significantly affected by the porosity, pore size, and factors such as the uniformity and size of the media, as recently revealed [37]. In addition, it is speculated that the retained OgCN itself may form an unstable permeable network with varying holding capacity of particles [38].

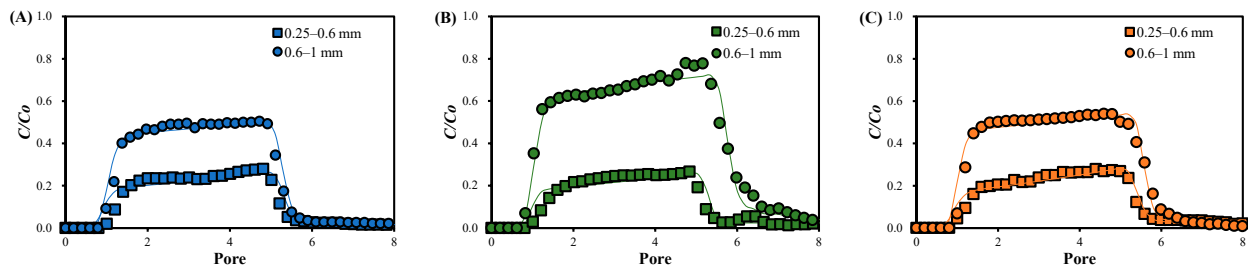


Figure 4. Experimental results and modeling breakthrough curves of the transport of OgCN of different concentrations in the column filled with quartz sands of different grain sizes: (A) 10 mg L⁻¹, (B) 50 mg L⁻¹, and (C) 100 mg L⁻¹. Flow rate = 5 mL min⁻¹, pH = 7 ± 0.2.

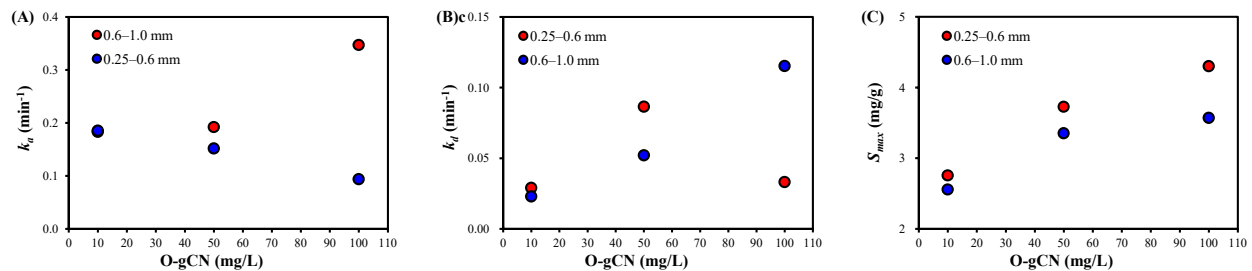


Figure 5. The correlations of OgCN concentration with (A) k_a , (B) k_d , and (C) S_{max} for 0.25–0.6 mm and 0.6–1.0 mm sand.

The S_{max} was similar for both sizes of sand when the OgCN concentration was 10 and 50 mg/L, with values of 2.56–2.76 and 3.35–3.73 mg/g, respectively, but it was higher in 0.25–0.6 mm sand (4.30 mg/g) than in 0.6–1.0 mm sand (3.57 mg/g), at 100 mg/L. This suggests that the attachment was improved while the detachment was suppressed in a medium of smaller pores above a certain input concentration of OgCN, i.e., 100 mg/L.

3.2.2. Effect of Ionic Strength

The breakthrough curves of OgCN at different IS are provided in Figure 6A, with the simulated curves, in relation to the volume of the O-gCN suspension passed through the column (V) divided by the pore volume of the column (V_0). The transport of OgCN was decreased as the IS was increased to 10 mM KCl. The parameters representing attachment (k_a) and retention (S_{max}) were increased, while the indicator of detachment (k_d) was decreased. The k_a and S_{max} were linearly correlated with IS (the concentration of KCl) with correlation coefficients (r^2) of 0.9917 and 0.9818, respectively. This strongly suggests that IS was directly correlated with the attachment and retention of OgCN in the medium in this study, i.e., quartz sand. On the other hand, the k_d was 0.0052 min⁻¹ when no KCl was added, but was decreased greatly to 0.0001–0.0017 min⁻¹ with 2–10 mM KCl. This indicates that the detachment of OgCN would be decreased dramatically under a low IS. Therefore, the increase in S_{max} with increasing IS was attributable to both enhanced attachment and suppressed detachment.

The enhanced attachment and suppressed detachment observed in the OgCN particles are associated with enhanced aggregation of OgCN particles and increased aggregate size. It was found that the zeta potential of OgCN was not notably affected at pHs of 2–5; however, it decreased significantly as the IS was increased at pHs of 6–7, where the experiments in this study were carried out (Figure 6B). The zeta potential was -39.28 ± 1.54 and -21.27 ± 6.58 mV when KCl concentrations were 0 (zero) and 10 mM, respectively. In addition, it was found via the PSD analysis of the aggregated OgCN particles in the suspensions at various IS, i.e., KCl concentration, that the average hydrodynamic diameter of the OgCN increased gradually from 1484.7 ± 127.4 to 2035.0 ± 209.1 μm as the KCl concentration increased from 0 (zero) to 10 mM (Figure 6C). This is attributable to the

compression of the electrical double layer on the surface of OgCN and the charge neutralization via the adsorption of ions with counter charge, which reduces the repulsion between OgCN particles [39,40], leading to increased retention of OgCN particles on the media as well as the aggregation of OgCN. The results in Figure 6 are compatible with Derjaguin–Landau–Verwey–Overbeek (DLVO) theory explanations, which proposed that electrostatic interactions played a detrimental role in regulating the transport of OgCN via controlling the colloidal stability and aggregation of OgCN [39,40].

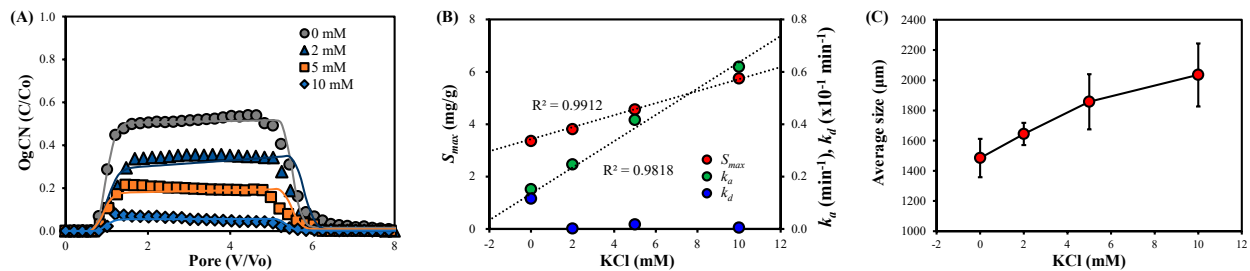


Figure 6. (A) Experimental and modeled breakthrough curves of OgCN with various IS and (B) the correlations of the parameters of the HYDRUS-1D model with IS. The flow rate was 5 mL min⁻¹, [OgCN] = 50 mg L⁻¹, pH = 7 ± 0.2. (C) The size of the OgCN aggregates with respect to IS (KCl concentration).

On the other hand, non-DLVO interactions, such as hydrogen bonding, would contribute to the results in Figure 6A [41]. It was reported that hydrogen bonding between the nitrogen lone pair electrons in gCN and Si-OH on quartz sand was promoted at high ISs. In addition, the deposited gCN provides new adsorption sites of gCN introduced later, via π - π conjugation [42]. It was also reported that the Debye length of gCN approaches the length of hydrogen bonds, i.e., 0.26–0.33 nm, with increasing IS, thus facilitating hydrogen bonding between quartz sand and gCN [42].

Meanwhile, the response of MWCNT to the raised IS was less sensitive compared with that of OgCN and differed from that of OgCN (Table 3). The S_{max} was increased from 2.69 to 3.43 mg/g when 10 mM KCl was used. However, the k_a did not show a notable change, while the k_d decreased greatly from 0.0023 to 0.0011 min⁻¹. These observations suggest that a decreased detachment, rather than increased attachment, was responsible for the enhanced retention of MWCNT, i.e., increased S_{max} is associated with increased IS.

4. Conclusions

In this study, OgCN and MWCNT were compared in terms of their characteristics and transport in porous media to identify the properties that would be beneficial for transport. Afterward, the transport of OgCN was investigated to evaluate the potential of its use in ISCO.

The transport of OgCN was much better than that of MWCNT, with less attachment and greater detachment. The OgCN contained more diverse and abundant O- and/or N-containing functional groups, such as graphitic C–C/C=C, C–O, C=O, N–C–N, C–N=C, and C₃–N, than MWCNT. In addition, OgCN contained more stacked, charged, disordered, defective, and amorphous graphitic structures than MWCNT. The transport of OgCN was well described using a 1-D ADR model (HYDRUS-1D), the parameters of which are provided. The S_{max} increased with increasing OgCN concentration, but the increase was not as significant as the increase in OgCN, and k_a and k_d were not always clearly dependent on the OgCN concentration and grain size of sand. These indicate that OgCN transport was influenced by a combination of attachment, detachment, and pore size. However, IS has clear and significant effects on transport via the reduction in zeta potential and the associated increase in the size of OgCN aggregates. MWCNT showed similar responses to raised IS, but they were not as sensitive as OgCN.

The results of this study contribute substantially to efforts to prepare more readily transportable materials and to establish proper strategies for the subsurface injection of materials for ISCO.

Author Contributions: Data curation, D.-G.K.; analysis, D.-G.K. and T.-T.N.; funding acquisition, S.-O.K.; investigation, D.-G.K. and T.-T.N.; methodology, D.-G.K. and T.-T.N.; project administration, S.-O.K.; writing—original draft, D.-G.K. and T.-T.N.; and writing—review and editing, D.-G.K. and S.-O.K. All authors have read and agreed to the published version of the manuscript.

Funding: This work was supported by a National Research Foundation of Korea (NRF) grant funded by the Korean government (MSIT) (No. 2022R1A2B5B02001584).

Data Availability Statement: The data presented in this study are available on request from the corresponding author.

Conflicts of Interest: The authors declare no conflict of interest.

References

1. Yan, H.; Lai, C.; Wang, D.; Liu, S.; Li, X.; Zhou, X.; Yi, H.; Li, B.; Zhang, M.; Li, L. In Situ Chemical Oxidation: Peroxide or Persulfate Coupled with Membrane Technology for Wastewater Treatment. *J. Mater. Chem. A Mater.* **2021**, *9*, 11944–11960. [[CrossRef](#)]
2. Calenciuc, C.; Fdez-Sanromán, A.; Lama, G.; Annamalai, S.; Sanromán, A.; Pazos, M. Recent Developments in Advanced Oxidation Processes for Organics-Polluted Soil Reclamation. *Catalysts* **2022**, *12*, 64. [[CrossRef](#)]
3. Devi, P.; Das, U.; Dalai, A.K. In-Situ Chemical Oxidation: Principle and Applications of Peroxide and Persulfate Treatments in Wastewater Systems. *Sci. Total Environ.* **2016**, *571*, 643–657. [[CrossRef](#)] [[PubMed](#)]
4. Matthaiou, V.; Oulego, P.; Frontistis, Z.; Collado, S.; Hela, D.; Konstantinou, I.K.; Diaz, M.; Mantzavinos, D. Valorization of Steel Slag towards a Fenton-like Catalyst for the Degradation of Paraben by Activated Persulfate. *Chem. Eng. J.* **2019**, *360*, 728–739. [[CrossRef](#)]
5. Arellano, M.; Sanroman, M.A.; Pazos, M. Electro-Assisted Activation of Peroxymonosulfate by Iron-Based Minerals for the Degradation of 1-Butyl-1-Methylpyrrolidinium Chloride. *Sep. Purif. Technol.* **2019**, *208*, 34–41. [[CrossRef](#)]
6. Xiao, S.; Cheng, M.; Zhong, H.; Liu, Z.; Liu, Y.; Yang, X.; Liang, Q. Iron-Mediated Activation of Persulfate and Peroxymonosulfate in Both Homogeneous and Heterogeneous Ways: A Review. *Chem. Eng. J.* **2020**, *384*, 123265. [[CrossRef](#)]
7. Wang, J.; Wang, S. Activation of Persulfate (PS) and Peroxymonosulfate (PMS) and Application for the Degradation of Emerging Contaminants. *Chem. Eng. J.* **2018**, *334*, 1502–1517. [[CrossRef](#)]
8. Li, L.; Huang, J.; Hu, X.; Zhang, S.; Dai, Q.; Chai, H.; Gu, L. Activation of Sodium Percarbonate by Vanadium for the Degradation of Aniline in Water: Mechanism and Identification of Reactive Species. *Chemosphere* **2019**, *215*, 647–656. [[CrossRef](#)]
9. Ribeiro, A.R.; Nunes, O.C.; Pereira, M.F.R.; Silva, A.M.T. An Overview on the Advanced Oxidation Processes Applied for the Treatment of Water Pollutants Defined in the Recently Launched Directive 2013/39/EU. *Environ. Int.* **2015**, *75*, 33–51. [[CrossRef](#)]
10. Thomas, N.; Dionysiou, D.D.; Pillai, S.C. Heterogeneous Fenton Catalysts: A Review of Recent Advances. *J. Hazard. Mater.* **2021**, *404*, 124082. [[CrossRef](#)]
11. Chatterjee, R.; Bhanja, P.; Bhaumik, A. The Design and Synthesis of Heterogeneous Catalysts for Environmental Applications. *Dalton Trans.* **2021**, *50*, 4765–4771. [[CrossRef](#)] [[PubMed](#)]
12. Zhao, Q.; Mao, Q.; Zhou, Y.; Wei, J.; Liu, X.; Yang, J.; Luo, L.; Zhang, J.; Chen, H.; Chen, H. Metal-Free Carbon Materials-Catalyzed Sulfate Radical-Based Advanced Oxidation Processes: A Review on Heterogeneous Catalysts and Applications. *Chemosphere* **2017**, *189*, 224–238. [[CrossRef](#)] [[PubMed](#)]
13. Oyekunle, D.T.; Zhou, X.; Shahzad, A.; Chen, Z. Review on Carbonaceous Materials as Persulfate Activators: Structure–Performance Relationship, Mechanism and Future Perspectives on Water Treatment. *J. Mater. Chem. A Mater.* **2021**, *9*, 8012–8050. [[CrossRef](#)]
14. Zhu, K.; Shen, Y.; Hou, J.; Gao, J.; He, D.; Huang, J.; He, H.; Lei, L.; Chen, W. One-Step Synthesis of Nitrogen and Sulfur Co-Doped Mesoporous Graphite-like Carbon Nanosheets as a Bifunctional Material for Tetracycline Removal via Adsorption and Catalytic Degradation Processes: Performance and Mechanism. *Chem. Eng. J.* **2021**, *412*, 128521. [[CrossRef](#)]
15. Zhang, P.; Tan, X.; Liu, S.; Liu, Y.; Zeng, G.; Ye, S.; Yin, Z.; Hu, X.; Liu, N. Catalytic Degradation of Estrogen by Persulfate Activated with Iron-Doped Graphitic Biochar: Process Variables Effects and Matrix Effects. *Chem. Eng. J.* **2019**, *378*, 122141. [[CrossRef](#)]
16. Lin, K.-Y.A.; Zhang, Z.-Y.; Wi-Afedzi, T. Sulfur-Doped Carbon Nitride as a Non-Metal Heterogeneous Catalyst for Sulfate Radical-Based Advanced Oxidation Processes in the Absence of Light Irradiation. *J. Water Proc. Eng.* **2018**, *24*, 83–89. [[CrossRef](#)]
17. Kohantorabi, M.; Moussavi, G.; Giannakis, S. A Review of the Innovations in Metal-and Carbon-Based Catalysts Explored for Heterogeneous Peroxymonosulfate (PMS) Activation, with Focus on Radical vs. Non-Radical Degradation Pathways of Organic Contaminants. *Chem. Eng. J.* **2021**, *411*, 127957. [[CrossRef](#)]
18. Gao, Y.; Zhu, Y.; Lyu, L.; Zeng, Q.; Xing, X.; Hu, C. Electronic Structure Modulation of Graphitic Carbon Nitride by Oxygen Doping for Enhanced Catalytic Degradation of Organic Pollutants through Peroxymonosulfate Activation. *Environ. Sci. Technol.* **2018**, *52*, 14371–14380. [[CrossRef](#)]

19. Nguyen, T.T.; Kim, D.G.; Ko, S.O. Changes in the Catalytic Activity of Oxygen-Doped Graphitic Carbon Nitride for the Repeated Degradation of Oxytetracycline. *Chemosphere* **2022**, *307*, 135870. [[CrossRef](#)]
20. Tang, R.; Ding, R.; Xie, X. Preparation of Oxygen-Doped Graphitic Carbon Nitride and Its Visible-Light Photocatalytic Performance on Bisphenol A Degradation. *Water Sci. Technol.* **2018**, *78*, 1023–1033. [[CrossRef](#)]
21. Qiu, P.; Xu, C.; Chen, H.; Jiang, F.; Wang, X.; Lu, R.; Zhang, X. One Step Synthesis of Oxygen Doped Porous Graphitic Carbon Nitride with Remarkable Improvement of Photo-Oxidation Activity: Role of Oxygen on Visible Light Photocatalytic Activity. *Appl. Catal. B* **2017**, *206*, 319–327. [[CrossRef](#)]
22. O'Carroll, D.M.; Liu, X.; Mattison, N.T.; Petersen, E.J. Impact of Diameter on Carbon Nanotube Transport in Sand. *J. Colloid Interf. Sci.* **2013**, *390*, 96–104. [[CrossRef](#)] [[PubMed](#)]
23. Wang, J.; Zhang, L.; Long, F.; Wang, W.; Gu, Y.; Mo, S.; Zou, Z.; Fu, Z. Solvent-Free Catalytic Synthesis and Optical Properties of Super-Hard Phase Ultrafine Carbon Nitride Nanowires with Abundant Surface Active Sites. *RSC Adv.* **2016**, *6*, 23272–23278. [[CrossRef](#)]
24. Šimůnek, J.; Van Genuchten, M.T.; Šejna, M. The HYDRUS Software Package for Simulating Two-and Three-Dimensional Movement of Water, Heat, and Multiple Solutes in Variably-Saturated Media. *Tech. Man. Version* **2006**, *1*, 241.
25. Fan, W.; Jiang, X.; Lu, Y.; Huo, M.; Lin, S.; Geng, Z. Effects of Surfactants on Graphene Oxide Nanoparticles Transport in Saturated Porous Media. *J. Environ. Sci.* **2015**, *35*, 12–19. [[CrossRef](#)]
26. Zhou, X.-L.; Liu, Z.-M.; Kiss, J.; Sloan, D.W.; White, J.M. Surface Chemistry of Chloriodomethane, Coadsorbed with H and O, on Pt(111). *J. Am. Chem. Soc.* **1995**, *117*, 3565–3592. [[CrossRef](#)]
27. Smith, M.; Scudiero, L.; Espinal, J.; McEwen, J.-S.; Garcia-Perez, M. Improving the deconvolution and interpretation of XPS spectra from chars by ab initio calculations. *Carbon* **2016**, *110*, 155–171. [[CrossRef](#)]
28. Meng, Y.; Li, Z.; Tan, J.; Li, J.; Wu, J.; Zhang, T.; Wang, X. Oxygen-Doped Porous Graphitic Carbon Nitride in Photocatalytic Peroxymonosulfate Activation for Enhanced Carbamazepine Removal: Performance, Influence Factors and Mechanisms. *Chem. Eng. J.* **2022**, *429*, 130860. [[CrossRef](#)]
29. Song, X.; Li, X.; Zhang, X.; Wu, Y.; Ma, C.; Huo, P.; Yan, Y. Fabricating C and O Co-Doped Carbon Nitride with Intramolecular Donor-Acceptor Systems for Efficient Photoreduction of CO₂ to CO. *Appl. Catal. B* **2020**, *268*, 118736. [[CrossRef](#)]
30. Majdoub, M.; Anfar, Z.; Amedlous, A. Emerging Chemical Functionalization of G-C₃N₄: Covalent/Noncovalent Modifications and Applications. *ACS Nano* **2020**, *14*, 12390–12469. [[CrossRef](#)]
31. Çelik, A.; Özer, H.Ö.; Tüzemen, Ş.M.; Yıldız, M.; Kovacı, H. Synthesis, characterization and tribological properties of solid lubricant graphite films produced by PECVD. *Mater. Today Comm.* **2023**, *36*, 106506. [[CrossRef](#)]
32. Jaworski, S.; Wierzbicki, M.; Sawosz, E.; Jung, A.; Gielerek, G.; Biernat, J.; Jaremek, H.; Łojkowski, W.; Woźniak, B.; Wojnarowicz, J. Graphene Oxide-Based Nanocomposites Decorated with Silver Nanoparticles as an Antibacterial Agent. *Nanoscale Res. Lett.* **2018**, *13*, 116. [[CrossRef](#)] [[PubMed](#)]
33. Sadezky, A.; Muckenhuber, H.; Grothe, H.; Niessner, R.; Pöschl, U. Raman Microspectroscopy of Soot and Related Carbonaceous Materials: Spectral Analysis and Structural Information. *Carbon NY* **2005**, *43*, 1731–1742. [[CrossRef](#)]
34. Kim, Y.; Choi, K.; Jung, J.; Park, S.; Kim, P.-G.; Park, J. Aquatic toxicity of acetaminophen, carbamazepine, cimetidine, diltiazem and six major sulfonamides, and their potential ecological risks in Korea. *Environ. Int.* **2007**, *33*, 370–375. [[CrossRef](#)] [[PubMed](#)]
35. Kasel, D.; Bradford, S.A.; Šimůnek, J.; Heggen, M.; Vereecken, H.; Klumpp, E. Transport and Retention of Multi-Walled Carbon Nanotubes in Saturated Porous Media: Effects of Input Concentration and Grain Size. *Water Res.* **2013**, *47*, 933–944. [[CrossRef](#)] [[PubMed](#)]
36. Tian, Y.; Gao, B.; Morales, V.L.; Wang, Y.; Wu, L. Effect of Surface Modification on Single-Walled Carbon Nanotube Retention and Transport in Saturated and Unsaturated Porous Media. *J. Hazard. Mater.* **2012**, *239*, 333–339. [[CrossRef](#)] [[PubMed](#)]
37. Hashemi, A.; Nguyen, C.; Loi, G.; Khazali, N.; Yang, Y.; Dang-Le, B.; Russell, T.; Bedrikovetsky, P. Colloidal Detachment in Porous Media: Stochastic Model and Upscaling. *Chem. Eng. J.* **2023**, *474*, 145436. [[CrossRef](#)]
38. Bradford, S.A.; Simunek, J.; Bettahar, M.; Van Genuchten, M.T.; Yates, S.R. Modeling Colloid Attachment, Straining, and Exclusion in Saturated Porous Media. *Environ. Sci. Technol.* **2003**, *37*, 2242–2250. [[CrossRef](#)]
39. Park, C.M.; Chu, K.H.; Heo, J.; Her, N.; Jang, M.; Son, A.; Yoon, Y. Environmental Behavior of Engineered Nanomaterials in Porous Media: A Review. *J. Hazard. Mater.* **2016**, *309*, 133–150. [[CrossRef](#)]
40. Sumanasekera, G.U.; Chen, G.; Takai, K.; Joly, J.; Kobayashi, N.; Enoki, T.; Eklund, P.C. Charge Transfer and Weak Chemisorption of Oxygen Molecules in Nanoporous Carbon Consisting of a Disordered Network of Nanographene Sheets. *J. Phys. Condens. Matter* **2010**, *22*, 334208. [[CrossRef](#)]
41. Zhang, M.; Bradford, S.A.; Klumpp, E.; Šimůnek, J.; Wang, S.; Wan, Q.; Jin, C.; Qiu, R. Significance of Non-DLVO Interactions on the Co-Transport of Functionalized Multiwalled Carbon Nanotubes and Soil Nanoparticles in Porous Media. *Environ. Sci. Technol.* **2022**, *56*, 10668–10680. [[CrossRef](#)] [[PubMed](#)]
42. Jiang, Y.; Guan, D.; Liu, Y.; Yin, X.; Zhou, S.; Zhang, G.; Wang, N.; Sun, H. The Transport of Graphitic Carbon Nitride in Saturated Porous Media: Effect of Hydrodynamic and Solution Chemistry. *Chemosphere* **2020**, *248*, 125973. [[CrossRef](#)] [[PubMed](#)]

Disclaimer/Publisher's Note: The statements, opinions and data contained in all publications are solely those of the individual author(s) and contributor(s) and not of MDPI and/or the editor(s). MDPI and/or the editor(s) disclaim responsibility for any injury to people or property resulting from any ideas, methods, instructions or products referred to in the content.